Advanced Functional Materials

ADVANCED FUNCTIONAL MATERIALS
www.afm-journal.de

RESEARCH ARTICLE OPEN ACCESS

Non-Monotonic Changes in the Thermal Conductivity of Conjugated Polymer Films with Increasing Levels of Chemical Doping

Reid W. Wilson[1] | Xinping Shi[2] | Diego Garcia Vidales[1] | Abigail Slimp[1] | Zerina Mehmedović[1] | Alexander F. Simafranca[1] | Eric C. Wu[1] | Sarah H. Tolbert[1,3] | Richard B. Wilson[2,4] | Benjamin J. Schwartz[1]

[1]Department of Chemistry and Biochemistry, University of California, Los Angeles, California, USA | [2]Department of Mechanical Engineering, University of California, Riverside, California, USA | [3]Department of Materials Science and Engineering, University of California, Los Angeles, California, USA | [4]Materials Science and Engineering, University of California, Riverside, California, USA

Correspondence: Benjamin J. Schwartz (schwartz@chem.ucla.edu)

Received: 12 February 2026 | **Revised:** 17 June 2026 | **Accepted:** 18 June 2026

Keywords: conjugated polymers | density | doping | heat capacity | thermal conductivity | thermoelectric efficiency | time-domain thermoreflectance

ABSTRACT

The performance of thermoelectric materials is characterized by the figure of merit (zT), which depends on knowing the thermal conductivity (κ). Poly(3-hexylthiophene-2,5-diyl) (P3HT) films doped with 2,3,5,6-tetrafluoro-7,7,8,8-tetracyano-quinodimethane (F_4TCNQ) are a prototypical conjugated polymer system studied for potential use in thermoelectrics. However, the few reports for this system disagree as to whether κ increases or decreases upon doping. This disagreement is partly due to the use of measurement techniques that rely on knowing the volumetric heat capacity (C_v) to determine κ, even though the C_v of conjugated polymers has not been systematically investigated as a function of doping. Here, we experimentally determine both C_v, using differential scanning calorimetry and careful density measurements, and thermal effusivity, using time-domain thermoreflectance (TDTR), to reveal how the κ of both regioregular and regiorandom P3HT changes as a function of doping with F_4TCNQ. Our results show that both C_v and κ change non-monotonically with the intercalated F_4TCNQ:thiophene monomer ratio. At low doping ratios, κ increases because of doping-induced crystal structure changes, while at higher doping ratios, κ decreases because of the increasing density of F_4TCNQ^- counterions in the crystal lattice. We find that F_4TCNQ-doped P3HT films can achieve zT values of 5.2×10^{-3}.

1 | Introduction

Doped semiconducting polymers are being developed as materials for thermoelectric applications due to their chemical tunability, mechanical flexibility, and material affordability [1, 2]. The thermoelectric energy conversion efficiency is typically quantified using the figure of merit, zT, which involves the electrical conductivity, σ, the Seebeck coefficient, S, and the thermal conductivity, κ, of a material via [3–5]:

$$zT = \frac{\sigma S^2}{\kappa} T \tag{1}$$

where T is the absolute temperature, introduced into Equation (1) to make zT dimensionless. Much of the last few decades of work on doped conjugated polymer-based systems has focused on strategies to improve the power factor [6, 7], σS^2. Since increased doping levels tend to increase σ and reduce S, there is typically a doping level 'sweet spot' that maximizes the power factor.

However, there are very few studies that have examined the κ of either *p*- or *n*-doped conjugated polymers [8–34], so there is relatively little knowledge of how zT changes with doping for this promising class of materials.

The thermal conductivity is an intrinsic property of a material primarily composed of electronic (κ_{el}) and lattice (κ_{lat}) contributions [35], $\kappa = \kappa_{el} + \kappa_{lat}$, where charge carriers and lattice vibrations, respectively, serve as vehicles for heat transfer. Thermal conductivities of pristine (undoped) polymeric materials typically fall in the range of 0.1 – 1.0 W m^{-1} K^{-1} [36, 37], and processing techniques that enhance polymer chain alignment, such as mechanical stretching or nanoscale templating, can increase κ by multiple orders of magnitude [36, 38, 39]. Depending on the experimental method used [40], thermal conductivity measurements typically determine κ either in the cross-plane (perpendicular to the film) or in-plane (parallel to the film) direction. Although advanced techniques can be employed to determine both directions if in-plane values for κ are sufficiently high [41–45], this is not true for most polymer thin films. Because the polymer chains in both spin-coated and drop-cast films tend to lie in-plane [46, 47], polymers usually show a higher κ, or more efficient heat transfer, in the in-plane (along the chain) direction than in the cross-plane (perpendicular to the chain) direction [48–52].

One of the workhorse doped conjugated polymer systems studied for potential thermoelectric applications is poly(3-hexylthiophene-2,5-diyl) (P3HT; see Figure 1 for chemical structure) doped with 2,3,5,6-tetrafluoro-7,7,8,8-tetracyanoquinodimethane (F_4TCNQ; also see Figure 1 for chemical structure) [53–55]. Within the relatively few measurements of κ performed on chemically-doped conjugated polymer systems [8–34], several have focused on F_4TCNQ-doped P3HT [20–26]. Most of the work on F_4TCNQ-doped P3HT measured the cross-plane κ [20–23]. Disturbingly, the results from different groups not only do not agree as to the value of κ, but also do not agree as to whether doped P3HT has a higher [20, 23] or a lower [21, 22] κ compared to that of pristine P3HT. Among the few studies [24–26] that report an in-plane κ measurement for F_4TCNQ-doped P3HT, only Degousée et al. [24] compared the thermal conductivity of doped films to a pristine film, where an increase in κ upon doping was observed.

We believe that one of the main issues in determining accurate thermal conductivities for doped conjugated polymer films is that laser-based measurement methods directly probe either the thermal effusivity, r, or the thermal diffusivity, α. Both of these quantities are related to κ through the volumetric heat capacity, C_v:

$$r = \sqrt{\kappa \rho C_p} = \sqrt{\kappa C_v} = \frac{\kappa}{\sqrt{\alpha}} \quad (2)$$

where C_v is the product of the mass density, ρ, and the specific heat measured under constant pressure, C_p. Although published data on ρ and C_p exist for various types of pristine P3HT samples [22, 49, 51, 56–65] there has been no systematic study of how C_v (or even how either ρ or C_p) change in P3HT films as a function of the extent of F_4TCNQ doping. As far as we are aware, Ref. 22 provides the only reported C_p measurement in the literature for F_4TCNQ-doped P3HT, and there is no experimental data on how ρ changes with doping for P3HT films.

This lack of C_p and ρ measurements means that different groups measuring r or α have had to make differing assumptions regarding how C_v changes with doping to extract values of κ. For example, some studies [13–15, 20, 32] made the assumption that doped P3HT films (or various other doped semiconducting polymer systems) have identical C_v values to that of pristine P3HT (or to the pristine polymer at hand). Another study [21] approximated the C_v of F_4TCNQ-doped P3HT by extrapolating increases in C_p based on the measured increase in C_p reported in Ref. 22; these workers also estimated doped film densities by assuming that there was one F_4TCNQ dopant for every two P3HT unit cells. Still other studies [23–26] employed modeling to fit thermal resistivities (as opposed to r or α) in order to avoid the issue of how to treat C_v as a function of doping. Overall, we believe that the conflicting data in the literature about how the κ of conjugated polymers changes with doping arises because of the many different assumptions made about how C_v changes with doping.

To address both the conflicting reports of κ and the lack of C_v data in the literature, in this paper we combine values of cross-plane r, measured by time-domain thermoreflectance (TDTR) [41, 66–69], C_p, measured by differential scanning calorimetry (DSC) on samples of known mass, and ρ, determined directly as the mass/volume ratio, to accurately determine values for the cross-plane κ and zT for P3HT films as a function of the extent of doping by F_4TCNQ. Since regioregularity is known to influence the crystallinity, electronic structure, and thermoelectric properties of conjugated polymers [70–74], we also explore how κ changes for both regioregular (RR) and regiorandom (RRa) P3HT films over a wide range of doping levels. Additionally, we use grazing-incident wide-angle x-ray scattering (GIWAXS) to correlate doping-induced changes to C_v and κ with changes in the polymer crystal structure.

We find that the way C_v changes as a function of the extent of doping depends on the regioregularity of P3HT. For RR-P3HT films, C_v values of lightly-doped films start slightly lower than pristine RR-P3HT but gradually increase with higher doping levels, eventually surpassing the value of the pristine polymer. In contrast, RRa-P3HT films show a significant decrease in C_v upon doping because of the doping-induced conversion of amorphous polymer to more-ordered crystalline domains. When these C_v values are combined with TDTR measurements, we find that κ changes non-monotonically with F_4TCNQ doping, first increasing relative to that of pure P3HT upon light-to-moderate doping followed by a subsequent decrease in κ with heavier doping. By also measuring the electrical conductivity, σ, of the doped films, we determine that the non-monotonic changes in κ with doping result from changes that occur to κ_{lat} as opposed to κ_{el}, a direct result of doping-induced changes to the crystal structure of the P3HT films. Finally, we also measure the Seebeck coefficient, S, to monitor how zT changes with doping, which we find can reach values of 5.2×10^{-3} in F_4TCNQ-doped RR-P3HT films.

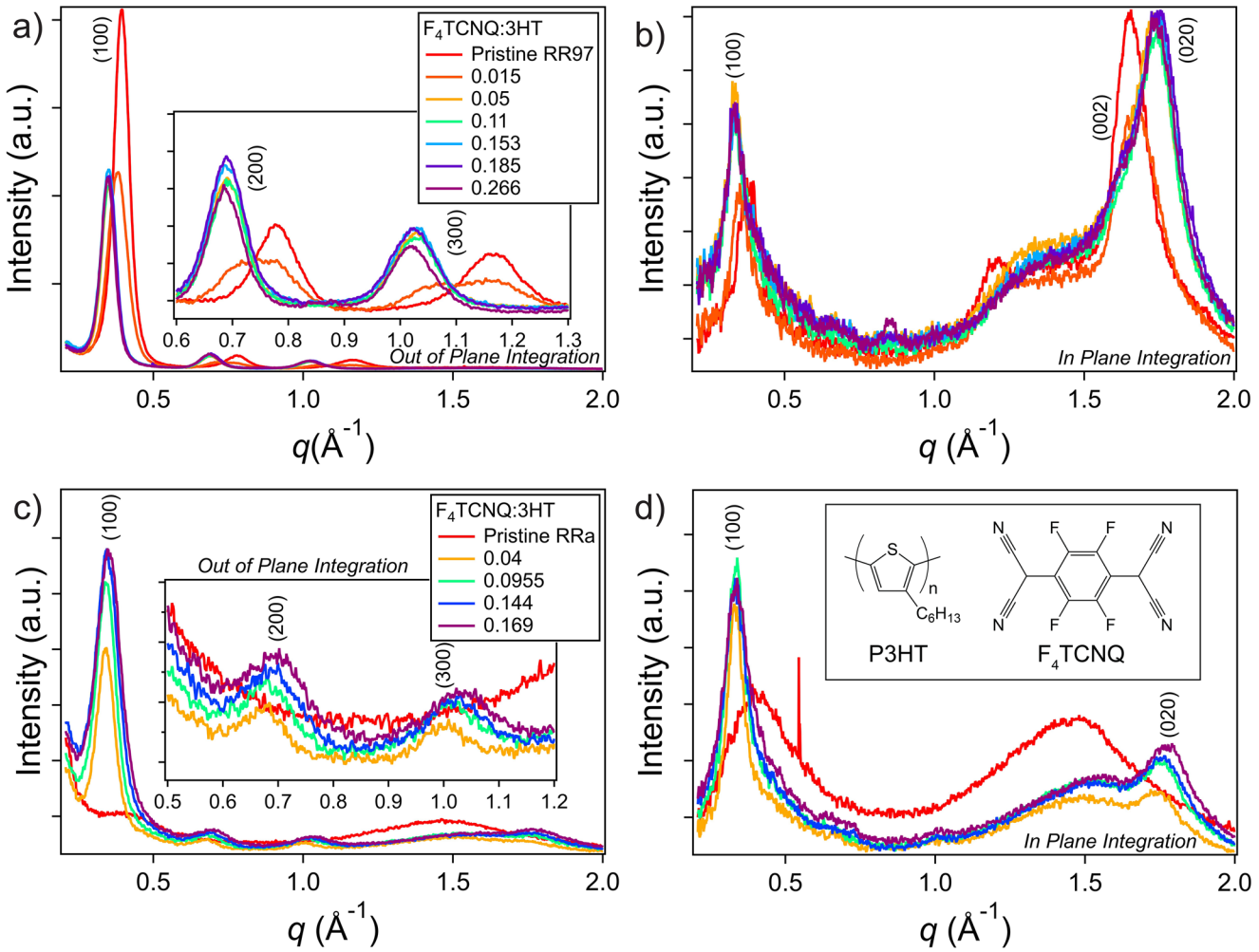

FIGURE 1 | Integrated pristine-film-thickness-normalized GIWAXS patterns for pristine and F_4TCNQ-doped RR-P3HT (a,b) and RRa-P3HT (c,d) films (see Figure S11 for the raw 2-D GIWAXS data). Figure 1a,c show out-of-plane integrations, which are dominated by the lamellar (h00) diffraction peaks, while Figure 1b,d show in-plane integrations, which show the (100) diffraction peaks with reduced intensity, as well as the monomer and π-stacking peaks, (00l) and (0k0), respectively. The data show that doping changes the crystal structure of the RR-P3HT films, and induces crystallization of the initially amorphous RRa-P3HT films. The inset in d shows the chemical structures of P3HT and F_4TCNQ.

2 | Results and Discussion

The overarching goal of this paper is to rigorously determine, using TDTR, how the cross-plane κ and zT of F_4TCNQ-doped P3HT films changes with the extent of F_4TCNQ doping. To accomplish this, accurate values for C_v of doped films must be determined to extract values of κ from the thermal effusivities measured with TDTR. The rest of this paper is organized as follows. With GIWAXS, we first articulate how doping with F_4TCNQ changes the crystal structure of P3HT films in Section 2.1. We then discuss in Sections 2.2 and 2.3 how C_p, ρ, C_v and κ vary as a function of doping, and to what extent the changes in these quantities are driven by structural and nonstructural factors. We find that in both RR-P3HT and RRa-P3HT films, the thermal conductivity changes non-monotonically, increasing at low doping concentrations compared to undoped films, followed by a subsequent decrease at higher doping concentrations. The highest zT value achieved was 5.2×10^{-3} for highly-F_4TCNQ-doped RR-P3HT, as discussed in Section 2.4. Overall, the results allow us to better understand the intertwined effects of how doping-induced changes to crystal structure and the introduction of molecular dopants impact thermal transport and the thermoelectric properties of F_4TCNQ-doped P3HT films.

Polymer films for GIWAXS, density measurements, TDTR, electrical conductivity measurements, and Seebeck measurements were prepared by spin-casting and doped via the sequential processing (SqP) method [75], a two-step process where the polymer film is cast onto a substrate prior to doping. The doping step involves exposing a pre-cast film to a dopant solution where the extent of doping can be controlled by the dopant concentration. The SqP doping method has been shown to yield films with more optimal thermoelectric properties than films prepared via the blend-doping method [75], where both polymer and dopant are cast from a single solution. To reach the minimum sample mass required for DSC measurements, polymer films for C_p determination were drop-cast rather than spin-cast. In drop-casting, films are made by allowing the solvent of a polymer solution to evaporate; this allows films to be made that are orders of magnitude thicker than spin-cast films. Doped films for C_p

measurements were prepared via the blend-doping method in order to precisely control the amount of F_4TCNQ. See Section 4.1, below, as well as Section S1.2 for additional sample preparation details.

Alongside direct measurements of mass and volume that were used to determine film densities, mass measurements of films taken before and after doping allowed us to also directly determine the amount of F_4TCNQ that intercalates within films doped via the SqP method (see Sections S1.3 and S1.4 for measurement details). This allowed for direct quantification of the mole ratio of F_4TCNQ-to-polymer thiophene monomer unit (3HT), as summarized in Table S1. For doped RRa-P3HT films, due to the loss of polymer during the SqP doping process (see Figure S2), we used a spectroscopy-based calibration method where measured film densities were used to determine the dopant:monomer mole ratios (see Section S1.4 and Figures S3 and S4).

2.1 | Measuring Crystal Structure Changes in F_4TCNQ-Doped RR- and RRa-P3HT Films via GIWAXS

Pristine RR-P3HT films are known to be semicrystalline, containing domains of ordered, π-stacked polymer, and more amorphous regions with less regular polymer stacking between the ordered domains. The presence of crystalline domains in both pristine and doped RR-P3HT films is apparent from the intense (h00) peaks in Figure 1a, which shows the out-of-plane integrated GIWAXS diffraction (for measurement details, see Section S1.9). In contrast, pristine RRa-P3HT shows only a weak (100) peak with no overtones, as seen in Figure 1c, indicating a film structure that is mostly amorphous. In the in-plane integrations (Figure 1b,d), the (h00) diffraction intensity is dramatically reduced, and peaks corresponding to the periodicity along the π-stacks (labeled (020)) and along the backbone of the polymer chain (monomer peak labeled (002)) appear. The facts that the out-of-plane (100) peak (Figure 1a) is significantly more intense than the in-plane (100) peak (Figure 1b) and that the (020) π-stacking peak and (002) monomer peaks lie primarily in-plane (Figure 1b) indicate that for RR-P3HT, the crystalline domains lie predominantly edge-on with respect to the substrate. The difference between in-plane and out-of-plane diffraction is slightly reduced for RRa-P3HT (Figure 1c,d), indicating reduced edge-on texture.

As RR-P3HT films are doped with F_4TCNQ, Figure 1a shows that the lamellar peaks shift to lower q, indicating an increase in the lamellar spacing and thus a volume expansion of the unit cell. This is because F_4TCNQ^- sits in the lamellar region of the crystallites between the side chains, so the crystal lattice must expand in this direction to make space for the counterion [76–81]. Indeed, for the lowest doping level (0.015:1 F_4TCNQ:3HT ratio) the (200) and (300) peaks are both clearly split in two, indicating a first-order phase transition and the co-existence of two distinct structures corresponding to doped and undoped crystallite populations [81]. As the doping level increases, the phase transition rapidly becomes complete, and the lamellar spacing then remains roughly constant as the doping level increases over a broad range (see Figure S12) [76]. Additionally, Figure 1b,d show that the initial doping-induced phase transition also causes the (020) π-stacking peak to shift to larger q (or smaller spacing—see Figure S13), the result of a change in chain tilt of the expanded unit cell [81]. The distance decrease in the π-stacking direction is much less than the increase in the lamellar direction, resulting in an overall increase in the unit cell volume. This means that the density of initially-doped P3HT should be smaller than that of pristine P3HT because of the large increase in unit cell volume caused by the doping-induced phase transition, as we detail further below.

The situation is somewhat different for RRa-P3HT, where doping induces crystallization of the initially-amorphous polymer [82, 83]. This doping-induced crystallization is easy to observe from the increase in diffraction intensity of both the lamellar and π-stacking diffraction peaks in the doped material, as seen Figure 1c,d. Doping-induced crystallization increases throughout the low- to moderate-doping regime before gradually reaching a limit at the highest doping levels tested, as seen by the growth of the integrated (100) peak area in Figure 1c and Figure S14. The doped lamellar and π-stack spacing distances for RRa-P3HT are quite similar to those of doped RR-P3HT (see Figures S12 and S13), with peaks that do not change position significantly with doping level, again indicating that the doped polymer structure is fixed with F_4TCNQ^- filling in open sites in the polymer lattice. This indicates that the doped film density should increase with doping level, as also discussed further below. It is worth noting that despite the doping-induced crystallization, the film-thickness-normalized integrated (100) peak areas are much smaller for RRa-P3HT than RR-P3HT across all doping levels (Figure S14), indicating net lower overall crystallinity in doped RRa-P3HT films. We expect that this difference in the crystalline-to-amorphous ratio of the two doped P3HT varieties will directly impact both the capacity of the respective polymer films to store heat (C_v) and transport it (κ).

2.2 | Determining C_v of RR- and RRa-P3HT as a Function of the Extent of F_4TCNQ-Doping

As mentioned above, to understand how doping-induced structural changes connect to the thermal conductivity, we need to have access to the volumetric heat capacity, C_v, to extract κ from the thermal effusivities measured by TDTR. Determining experimental values for C_v, in turn, requires taking the product of measured values for C_p and ρ, as per Equation (2).

2.2.1 | Measured Pristine and F_4TCNQ-doped RR- and RRa-P3HT Film Densities

As mentioned in the introduction, the way the density of F_4TCNQ-doped P3HT films changes with doping level has not been systematically studied in the literature, leaving κ studies that require C_v to either assume [20] pristine P3HT density values for doped films or extrapolate [21] increases in density based on estimated amounts of intercalated F_4TCNQ within the unit cell. The density of pristine P3HT, in contrast, has been examined in the literature using both experimental and computational methods [56–58], and most studies agree that the crystalline regions of RR-P3HT films have a density between 1.10–1.14 g cm^{-3} [56]. Given that the volumetric crystalline fraction of RR-P3HT samples has been estimated to be between 30%

and 90% [57, 59, 60], and that non-crystalline material should have a slightly lower density, overall film densities in the 1.10's g cm^{-3} are expected for RR material [57, 58]. Additionally, Refs. 57 and 58 suggest that the mass density remains practically constant for RR-P3HT as the molecular weight is varied. RRa-P3HT densities have been reported to be between 1.09–1.11 g cm^{-3} [56–58], which is consistent with the idea that amorphous P3HT has a marginally lower density than the more crystalline RR-P3HT.

Direct measurements of mass and volume (see the experimental procedure in Section S1.3) resulted in density values for pristine films of RR- and RRa-P3HT of 1.16(3) ± 0.04 and 1.10(3) ± 0.04 g cm^{-3}, respectively, which are the left-most points in Figure 2a (see also Figure S1), in good agreement with the literature described above. We also measured the bulk film density as a function of F_4TCNQ:3HT mole ratio for doped RR- and RRa-P3HT films by measuring the net gain in mass and increase in thickness of the films after doping. Since the solvent used in the doping solution can dissolve some of the pre-cast polymer, particularly with RRa-P3HT, we performed a calibration procedure that involved soak-doping and UV–vis-NIR spectroscopy to approximate the F_4TCNQ:3HT mole ratio for RRa-P3HT films doped using the SqP method, which is described in detail in Section S1.4. The data show that for F_4TCNQ-doped RR- and RRa-P3HT films (see also Figure S1), there is a roughly linear increase in density as additional dopant is incorporated into the polymer films. F_4TCNQ (molecular weight ≈276 g mol^{-1}) is heavier than a 3HT repeat unit (molecular weight ≈168 g mol^{-1}), so it is not surprising that a composite doped film that is ≈25% by mole dopant has a significantly higher density than a pristine polymer film.

We can understand the density changes upon doping in more detail by considering the doping-induced structural changes seen in the x-ray scattering data presented above. Based on its x-ray-determined unit cell volume of 466 Å^3, the crystalline fraction of pristine RR-P3HT should have a density of 1.20 g cm^{-3} (see section S1.4 for details). Since the measured density is 1.16 g cm^{-3}, this suggests that our pristine RR-P3HT films are ≈60% crystalline and ≈40% amorphous, presuming that the amorphous fraction has the same 1.10 g cm^{-3} density as RRa-P3HT. Given that we also know from x-ray scattering that the unit cell volume of the crystalline fraction of the RR-P3HT film increases to 518 Å^3 upon doping (as also detailed in Section S1.4) and that crystalline material is doped preferentially, the x-ray measurements thus predict an initial decrease in density upon doping. Then, as F_4TCNQ molecules begin to fill the expanded unit cell upon increased doping, the purple solid line in Figure 2a shows how the density would change given that there are no further structural changes and assuming that the crystalline fraction does not change upon doping. Clearly, our measured doped film densities agree well within error with the x-ray-predicted model, indicating that we have a good molecular understanding of the density of F_4TCNQ-doped RR-P3HT films. The fact that the density of the highest-doped sample we studied is a bit below the predicted value from the x-ray diffraction-based model is likely due to the fact that some lower-density amorphous material is also doped at this concentration.

To better estimate the density of the doped RR-P3HT films at lower doping levels, where it is hard to measure the mass

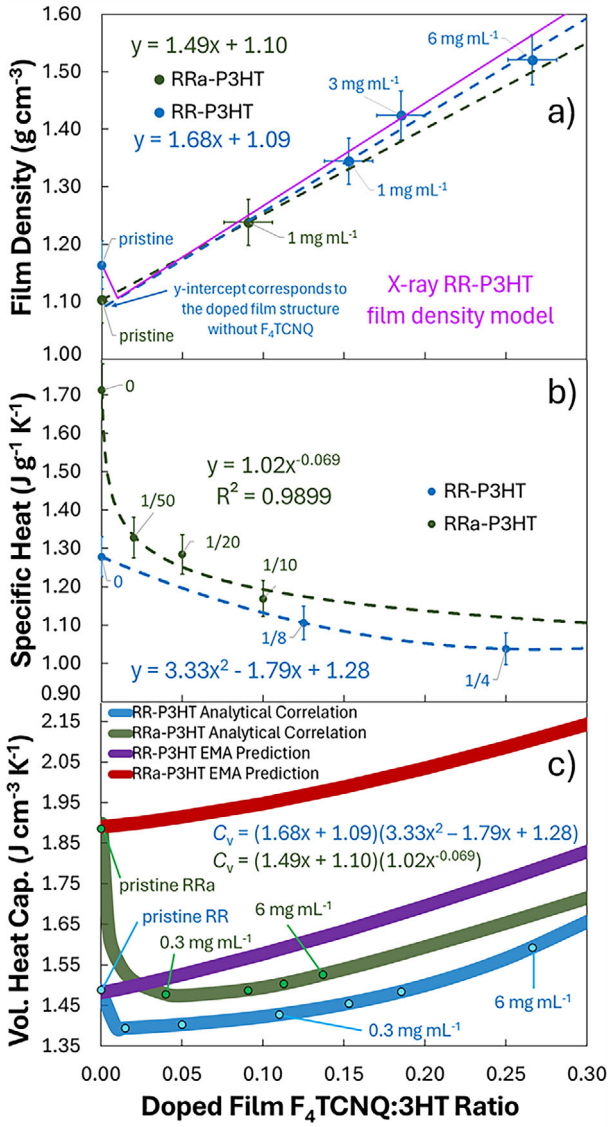

FIGURE 2 | (a) Measured bulk film densities of pristine and doped RR-P3HT (blue) and RRa-P3HT (green) films as a function of F_4TCNQ:3HT mole ratio; the dashed lines are fits to the data points; the F_4TCNQ doping concentrations used for the SqP doping method are indicated for each point. The purple solid line is a theoretical construct based on a model using the unit cell volume of the pristine and doped crystal structures from x-ray scattering. The blue dashed line is a fit to the measured data points assuming that the *y*-intercept has the expanded unit cell volume of the doped crystal structure rather than the higher-density pristine crystal structure (see Section S1.4 for details). (b) Measured specific heat, C_p, of pristine and doped RR- and RRa-P3HT films as a function F_4TCNQ:3HT doping ratio, along with analytic fits (dashed curves) to the data points. (c) Analytically-determined volumetric heat capacities, using the product of the fitting functions from panels (a) and (b), for RR- and RRa-P3HT films as a function of F_4TCNQ:3HT doping ratio. F_4TCNQ doping concentrations used in the SqP doping method are indicated for some points, with the full data given in Table S3. Effective medium approximation (EMA) calculations for doped RR-P3HT (purple curve) and RRa-P3HT (red curve) films using mole-fraction-weighted contributions of the bulk C_v values of F_4TCNQ and pristine RR- or RRa-P3HT. Clearly, the EMA fails to correctly predict the C_v of F_4TCNQ-doped P3HT, a direct result of the doping-induced structural changes that alter the heat capacity of the composite doped systems.

change by direct weighing, we linearly fit the measured points in Figure 2a, but forced the *y*-intercept to have a value that would correspond to the density of a hypothetical expanded (doped) structure, as determined from the x-ray model (see section S1.4), but without any F_4TCNQ in the lattice; this fit is shown as the blue dashed line. We then used the measured 1.16 g cm^{-3} density value of the pristine sample and the densities calculated using the blue dashed line for the doped RR-P3HT samples to determine C_v from C_p, as described further below.

We note that for P3HT, the doping efficiency (the ability of a dopant to generate a mobile carrier) of F_4TCNQ is 5%–18% [84–86], so that the F_4TCNQ:3HT ratio we measure is not equivalent to the carrier density. Instead, the ratio includes both intercalated F_4TCNQ^- ions that generate mobile carriers and F_4TCNQ species that form charge-transfer complexes or that produce carriers that are otherwise trapped in the film. We also note that RRa-P3HT is several hundred mV harder to dope than RR-P3HT, as it has a deeper valance band. As a result, we cannot achieve the same doping levels with RRa-P3HT as with RR-P3HT; this can be seen in Figure 2a by noting how different the F_4TCNQ:3HT ratios are when doping with the same F_4TCNQ solution (1 mg mL^{-1}). However, since the doped crystal structures of the two materials are similar, the way the density of the two materials changes with increasing doping level should also be similar, as we observe.

2.2.2 | Measured Pristine and F_4TCNQ-doped RR- and RRa-P3HT C_p Values

Specific heat measurements show that pristine P3HT samples with higher degrees of crystallinity tend to have lower specific heats [59, 61]. For example, a compilation of RR-P3HT samples of varying M_w (10.5–87 kg mol^{-1}) and polydispersity index (PDI) measured with DSC at 20°C shows that C_p values fall between a range of 1.3–1.6 J g^{-1} K^{-1} [49, 51, 59–64], whereas RRa-P3HT has C_p values between 1.72–1.95 J g^{-1} K^{-1} [59, 61, 65]. Apart from a single measurement by Kiefer et al. [22], who studied cold-pressed P3HT pellets and found a 12.8% increase in C_p upon doping with 20 mol% F_4TCNQ, C_p values for F_4TCNQ-doped P3HT have not been presented in the literature. The lack of data has led groups either to assume that C_p does not change from its pristine value upon doping [20], or to extrapolate [21] the result presented by Kiefer et al. [22]

To remedy this situation, we performed DSC measurements on drop-cast pristine RR- and RRa-P3HT films of known mass, shown as the left-most points in Figure 2b and the calorimetric traces in Figure S5 in Section S1.5. The values we obtained fall within the ranges found in the literature [49, 51, 59–65]. The fact that RRa-P3HT has a higher C_p than RR-P3HT, and knowing that each material has: 1) a similar number density of atoms per unit volume (a proxy to ρ, as discussed above); and 2) the same average mass per atom, reinforces the idea that having more structural disorder allows for a higher number of molecular degrees of freedom and thus a higher specific heat.

We then performed DSC on blend-cast F_4TCNQ-doped RR-P3HT films with varying amounts of dopant at controlled F_4TCNQ:3HT mole ratios, as shown in the calorimetric traces in Figures S6 and S7. We find that C_p decreases with increasing F_4TCNQ:3HT mole ratio, as seen in Figure 2b, a result that stands in contrast to that reported in Ref. 22. We measured bulk F_4TCNQ to have a C_p that is the same, within error, as RR-P3HT (see Figure S5), which suggests that the C_p drop in the doped films is not directly caused by F_4TCNQ having a different specific heat, but instead due to changes in the crystal structure that reduce the number of thermally-excitable degrees of freedom relative to the pristine polymer. We also see in Figure 2b that the C_p of F_4TCNQ-doped RRa-P3HT rapidly decreases upon initial doping and then decreases more slowly at higher doping concentrations. We believe that the larger initial drop in C_p of RRa-P3HT films upon doping is due to doping-induced crystallization (cf. Figure 1c,d) [82, 83], as the creation of new crystallites should lower the number of thermally accessible degrees of freedom available to the material.

2.2.3 | Pristine and F_4TCNQ-doped RR- and RRa-P3HT C_v Values

Most studies in the literature that required C_v values for pristine P3HT films in order to extract thermal conductivities typically either referenced outside measurements [21, 87, 88] for ρ and C_p or performed measurements of only one or the other of these two variables (see Table S6 for a compilation of studies) [20, 22, 49, 51, 63]. The fact that nearly every such study utilized inconsistent ρ and/or C_p values for pristine RR-P3HT resulted in values for C_v that ranged from 1.22–2.08 J cm^{-3} K^{-1} (see Table S6). On the other hand, as far as we are aware, the C_v of pristine RRa-P3HT has only been presented once in the literature, at 1.84 J cm^{-3} K^{-1}, based on external ρ and C_p values [21]. For F_4TCNQ-doped P3HT films, Zhao et al. [20] assumed that the C_v of doped P3HT remained unchanged from the pristine polymer, while Kiefer et al. [22] and Plunkett et al. [21] both suggested that C_v increases upon doping (see Section S2.1 for a detailed description of the C_v assignments made in Refs. 21 and 22).

Here, we analytically determine C_v values for pristine and F_4TCNQ-doped P3HT films by fitting our measured ρ and C_p data to analytic functions, as seen in Figure 2a,b, and then multiplying the two functions, as summarized in Figure 2c and Section S1.6. We find that the C_v's of pristine RR- and RRa-P3HT films are 1.49 and 1.89 J cm^{-3} K^{-1}, respectively, as seen via the left-most points in Figure 2c. The higher C_v of RRa-P3HT is due to the intrinsic disorder of the amorphous film, while in RR-P3HT films, the presence of crystalline domains results in a comparatively lower number of thermally excited degrees of freedom per unit volume. As RR-P3HT is doped with F_4TCNQ, C_v immediate decreases slightly due to the volume expansion that occurs within the crystalline domains of the film, the result of the doping-induced phase transition described above. C_v then slowly increases as more F_4TCNQ enters the film at higher doping levels, eventually surpassing the value of pristine RR-P3HT at roughly the 1:5 F_4TCNQ:3HT ratio. As RRa-P3HT is doped, however, a much more significant decrease in C_v occurs at low F_4TCNQ:3HT mole ratios due to doping-induced crystallization, as discussed above. The small increases in C_v at the highest doping levels of both P3HT varieties is believed to be driven by additional thermally-excitable degrees of freedom introduced by the increasing number of dopant molecules within the unit cell.

We can also compare our experimentally-derived C_v values to those expected from the effective medium approximation (EMA), which is commonly used to estimate the physical properties of composite materials. In the EMA, the C_v of doped P3HT can be estimated using the mole-fraction-weighted contributions of the C_v's of bulk F_4TCNQ (2.3 J cm^{-3} K^{-1}, which is the product of ρ, 1.57 g cm^{-3} [89], and our measured C_p) and the pristine polymer; these estimates are shown as the purple and red curves in Figure 2c for RR- and RRa-P3HT, respectively. Since the C_v of bulk F_4TCNQ is larger than that of both P3HT varieties, the EMA predicts an increase in C_v as the F_4TCNQ:3HT ratio increases, thus significantly overestimating C_v across nearly all doping levels. This is because the EMA does not account for doping-induced changes to the polymer's crystal structure, which leads to significant changes in C_p (for RR- and RRa-P3HT) and ρ (for RR-P3HT only). Therefore, the use of the EMA to estimate C_v in doped conjugated polymers, as was done in Ref. 21, is likely to lead to significant errors.

2.3 | Determination of κ as a Function of RR- and RRa-P3HT and F_4TCNQ-Doping

With experimentally-derived C_v values in-hand, we next determine cross-plane thermal conductivities using time-domain thermoreflectance for films of pristine and F_4TCNQ-doped RR- and RRa-P3HT. The thermal modeling implemented (see Section S1.7 for details) combines TDTR-measured thermal effusivities (r) with the above-determined volumetric heat capacities (C_v) to back out values for κ.

2.3.1 | Measured Pristine RR- and RRa-P3HT κ Values

In the literature, cross-plane κ measurements on non-aligned pristine P3HT have been performed using thermoreflective (TDTR/FDTR) [21, 87, 88, 90], photoacoustic (PA) [91], and electro-thermal (3ω, TET/PLTR2, TWA, Hot Disk TPS, Flash-DSC) [20, 22, 23, 49–51, 63, 92, 93] techniques. Although high-frequency laser-based and electrothermal methods require a C_v value, techniques in the low-frequency regime (particularly 3ω) [23, 24, 50, 92] do not require C_v to be known as thermal resistivities are directly measured [94, 95]. We note, however, that electro-thermal methods such as 3ω do not work well when the material of interest is electrically conductive, as is the case for doped conjugated polymers; they require an electrical insulator between the electrode and thin-film, which can then affect the resulting thermal measurement. In Table S6, we provide a list of cross-plane κ studies on pristine P3HT films tabulated by measurement technique, film processing method, P3HT type, the value of C_v used in extracting κ (if any) and the final estimated κ value. The range of published cross-plane κ values for pristine P3HT films spans 0.05–0.83 W m^{-1} K^{-1}, well over an order of magnitude, and the reasons for the wide range in κ are not entirely easy to decipher (see Section S2.2 for an analysis of how polymer properties and film processing techniques may impact κ and, beyond C_v assignments, likely contribute to the wide range of reported values).

Here, we measure a higher cross-plane κ for pristine RR-P3HT films, 0.31(1) ± 0.02(3) W m^{-1} K^{-1}, than for pristine RRa-P3HT, 0.22(7) ± 0.01(7) W m^{-1} K^{-1}, as shown by the left-most points in Figure 3 (Figure S8b shows an example of the thermal model fitted to data). We selected both P3HT varieties to have roughly the same molecular weight (see Section 4.1) to ensure that the percent regioregularity alone is the reason behind differences in the κ. Our measurements agree with reports in the literature that show that κ increases with the degree of polymer regioregularity [21, 92]. Since undoped P3HT has no charge carriers to transport heat, the changes to κ with regioregularity must be vibrational in nature, indicating that κ_{lat} increases with greater film crystallinity, as shown by our GIWAXS data for pristine RR- and RRa-P3HT in Section 2.1.

2.3.2 | Measured F_4TCNQ-doped RR- and RRa-P3HT κ Values

Cross-plane κ measurements on F_4TCNQ-doped P3HT in the literature have been performed much less frequently than pristine P3HT samples, although both thermoreflective (TDTR) [21] and electrothermal (3ω, Flash-DSC, Hot Disk/TPS) [20, 22, 23] measurements have been presented (see Table S7 for a summary of the reported data). Refs. 21 and 22, both of which published results on films doped to a single level alongside pristine films, reported a doping-induced 20%–50% decrease in κ. In contrast, Refs. 20 and 23, which measured κ across a variety of doping levels, reported a roughly 60% initial increase in κ upon doping compared to pristine P3HT samples. Additionally, Ref. 20 saw κ decrease as higher doping levels were reached, while Ref. 23 did not see any drop in κ at the highest doping levels investigated.

The results of our TDTR measurements show that the κ of both F_4TCNQ-doped RR- and RRa-P3HT changes non-monotonically as a function of the extent of doping, as seen in Figure 3. P3HT varieties show a rise in κ at low doping levels compared to their respective pristine films, followed by a lowering of κ at the highest doping levels tested. The non-monotonic trends of κ with doping level strongly suggests that there are at least two competing factors affecting thermal transport in doped P3HT films.

One possible explanation could involve competing changes in the electrical and lattice contributions underlying κ. The Weidmann-Franz law [96, 97], $\kappa_{el} = \sigma L_0 T$, where L_0 is the Lorenz number assigned as the Sommerfeld value, 2.44 × 10^{-8} W Ω K^{-2}, can be used to approximate the electronic contribution (κ_{el}) to the overall κ if the electrical conductivity, σ, is known. We measured the electrical conductivities of our doped P3HT samples, shown in Figure 4a, with additional details presented in Section S1.8. The highest σ we measured across all of our doped P3HT films was 7.9 S cm^{-1}, which means based on the Weidmann-Franz law that κ_{el} can be no more than 0.006 W m^{-1} K^{-1} (see Table S4 for κ_{el} approximations at each doping level). This value represents less than 10% of the observed increases in κ with doping, which leads us to conclude that the changes in κ across all doping levels must come from changes in κ_{lat}. This idea also agrees with literature claims that the κ of doped semiconducting polymers with low σ (<10 S cm^{-1}) is entirely influenced by κ_{lat} [30, 98, 99].

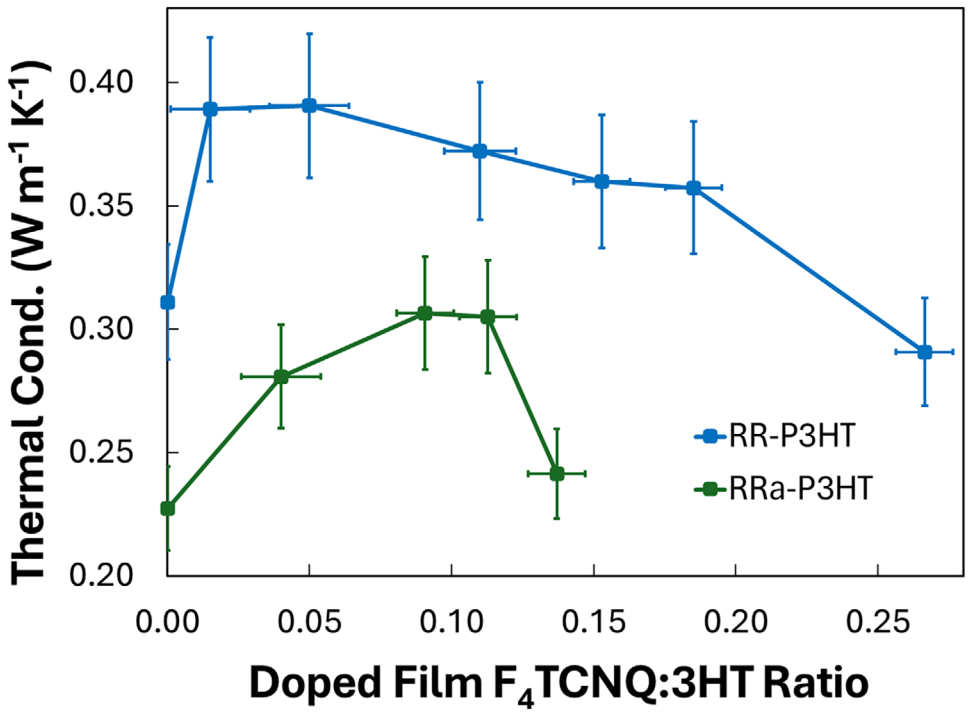

FIGURE 3 | Thermal conductivities, determined from effusivities (see Figure S9) measured via TDTR and the C_v values in Figure 2c, of doped RR- and RRa-P3HT films as a function of F_4TCNQ:3HT doping ratio. Non-monotonic changes to the thermal conductivity are observed with increasing doping level, with κ increasing upon light doping and then decreasing upon further doping. Thermal diffusivities plotted as a function of F_4TCNQ:3HT ratio are also displayed in Figure S10.

Thus, the initial increases in κ we observe at low F_4TCNQ:3HT mole ratios in RR-P3HT films and low-to-moderate ratios in RRa-P3HT films are due to doping-induced crystal structure changes that alter κ_{lat}. For RR-P3HT, the initial increase in κ with doping through the 0.05:1 F_4TCNQ:3HT mole ratio level is correlated with the doping-induced phase transition that occurs within the same doping regime, as mentioned above and documented in Figures S12 and S13. This phase transition also decreases the film paracrystallinity and increases the crystalline coherence length (Figure S16). For RRa-P3HT, the increase of κ with doping through the 0.1:1 F_4TCNQ:3HT mole ratio tracks closely with increasing levels of doping-induced crystallization, as also discussed above and shown in Figure S14. To understand the non-monotonic dependence of cross-plane κ on doping level, we consider different theories of thermal transport.

In kinetic-gas theory, κ depends on the number of thermally excited vibrational modes, their velocities, and their scattering rates. One interpretation of our results in Figure 3 is that pristine P3HT lies at or near the amorphous minimum-thermal conductivity limit described by the Cahill-Pohl model [100–103]. Low levels of doping increase structural order and coherence, as supported by the GIWAXS in Section 2.1, allowing vibrational modes with longer wavelengths than the minimum mean-free-path limit to propagate. Once RR- and RRa-P3HT films take on doped structures, the lack of decrease in C_v across varying doping levels, as seen in Figure 2c, rules out a large decrease in thermally populated vibrational degrees of freedom. Therefore, within kinetic-gas theory, the κ trend from low to high film F_4TCNQ:3HT ratios must primarily reflect changes in vibrational velocities, scattering rates, or both. In the absence of structural changes at high doping levels (as seen in Section 2.1), heavier doping adds local mass and force constant disorder through F_4TCNQ^- incorporation. This local disorder increases scattering rates and pushes mean-free-paths back toward the amorphous minimum-conductivity limit.

The Allen-Feldman framework for transport in amorphous solids yields a similar microscopic explanation for the non-monotonic cross-plane κ trend. In the Allen-Feldman framework [104, 105], heat-carrying vibrations are classified along a spectrum from highly mobile, extended modes to strongly localized ones. Our results imply that the structure changes that occur as pristine P3HT films are lightly doped with F_4TCNQ allow modes to have greater diffusivities and/or longer propagation distances. Then, increases in the F_4TCNQ:3HT ratio at higher doping levels cause vibrational modes to become more localized. It makes sense that incorporating F_4TCNQ dopant anions into the P3HT crystallites, which have very different vibrational frequencies than the surrounding polymer (e.g., the exterior of the dopant molecule consists of C-F and C≡N bonds), serve to further localize the vibrational modes that are responsible for thermal transport. For RRa-P3HT, the decrease in κ only occurs after doping-induced crystallization is complete, which occurs at roughly 0.11:1 F_4TCNQ:3HT, as seen in Figure S15.

We note that our view of increased mode scattering (kinetic-gas theory) or increased mode localization (Allen-Feldman framework) caused by the presence of dopant counterions stands in contrast to that of Guo et al., [32], who claimed that the cross-plane κ decrease seen upon doping conjugated polymers

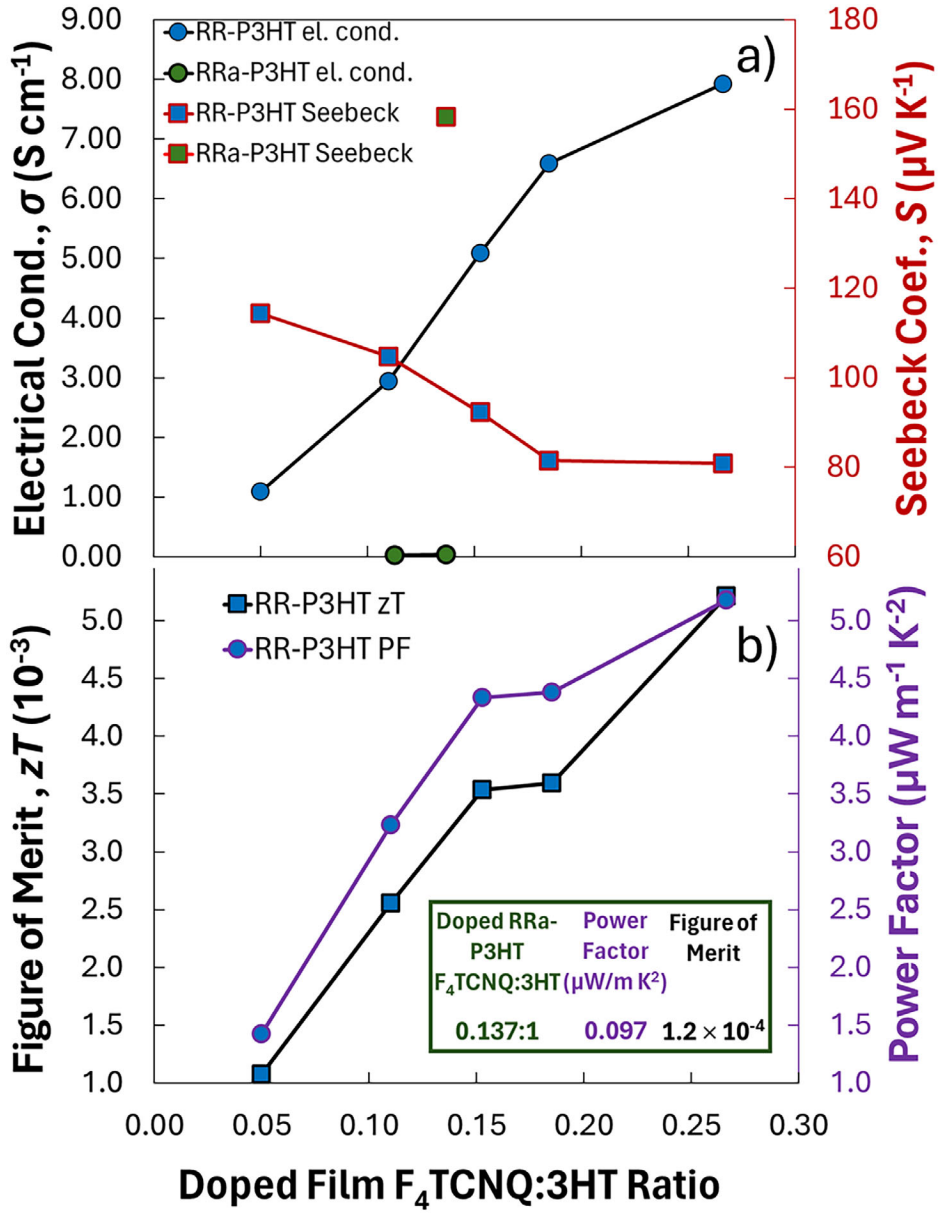

FIGURE 4 | (a) Electrical conductivity (black lines connected to circular data points) and Seebeck coefficient (red lines connected to square data points) plotted as a function of F_4TCNQ:3HT mole ratio for RR-P3HT (blue data points) and RRa-P3HT (green data points). (b) Figure of merit zT (black lines connected to square data points) and power factor values (purple lines connected to circular data points) for F_4TCNQ-doped RR-P3HT (blue data points). Only the most-doped RRa-P3HT film had a measurable Seebeck coefficient, so only this film has a reported power factor and zT value (see inset table outlined in green).

is due entirely to the lattice expansion of the unit cell within crystalline regions. Here, however, we see in Figure 3 that the doping-induced lattice expansion actually enhances the cross-plane κ.

Overall, we believe that the conflicting literature reports of increases and decreases to κ upon doping P3HT can be understood based on our finding of non-monotonic changes in thermal transport with doping. The competing effects are: 1) doping-induced changes to the crystal structure, which occur at low doping levels leading to increases in κ); and 2) increased mode localization due to the increasing number of F_4TCNQ^- ions in the lattice at high doping levels, resulting in a decrease in κ. For example, when Zhao et al.'s κ data on doped RR-P3HT is plotted as a function of F_4TCNQ:3HT ratio [20], as seen in Figure S17, the rise and fall in κ closely resembles the nonmonotonic trend observed in our measurements in Figure 3. In addition, Takayama et al.'s data on doped RR-P3HT [23], which saw an increase in κ upon doping without any decrease at higher doping levels, also mirrors our data in Figure 3 because all of their samples remained in the low-doping regime (based on their reported σ). Both Keifer et al. and Plunkett et al. found that κ decreases when RR-P3HT was doped with F_4TCNQ [21, 22], but the samples in these works were all heavily doped (≥0.2:1 F_4TCNQ:3HT mole ratios), at the high end of what we show in Figure 3. If Ref. 21's value for κ is adjusted to reflect the film C_v we report in Figure 2c, then our κ data and those in Refs. 21 and 22 all converge to about 0.3 W m^{-1} K^{-1} for heavily-F_4TCNQ-doped

RR-P3HT. In Section S2.3, we present a more detailed comparison of literature-based κ results and our findings.

2.4 | Determination of zT for F_4TCNQ-Doped RR- and RRa-P3HT Films

The thermoelectric figure of merit zT (Equation (1)) allows a comparison of the efficiency of different thermoelectric systems. Most studies on doped polymers only report power factors, σS^2, due to the inherent difficulties of measuring κ. Maximizing only the power factor is equivalent to the assumption that the thermal conductivities of doped polymer films do not change with doping level. With our well-characterized values for cross-plane κ's in-hand, we can calculate values of zT for F_4TCNQ-doped P3HT films as a function of doping level. These calculations are upper bounds due to the fact that our measurements of σ and S are in-plane while our measurements of κ are cross-plane, and we expect in-plane values of κ to be higher than cross-plane values [24, 48–51].

Electrical conductivities (circles) and Seebeck coefficients (squares) of our F_4TCNQ-doped P3HT samples are plotted in Figure 4a, with additional details described in Section S1.8. As expected, σ increases while S decreases as P3HT films become more doped. In Figure 4b, the power factor of doped RR-P3HT (circles) shows an increase with increasing doping level. Figure 4b also shows zT (squares) as a function of F_4TCNQ:3HT ratio for doped RR-P3HT films, with the numerical data presented in Table S5. We are able to report zT only for the most heavily-doped RRa-P3HT film due to limitations in being able to reliably measure σ and S for the lower-doped samples. We find that the zT of doped RR-P3HT films is over an order of magnitude larger than that of the most-doped RRa film, primarily because RR-P3HT is significantly easier to dope.

The highest zT for F_4TCNQ-doped RR-P3HT that we found, 5.2×10^{-3}, which corresponds to the most heavily-doped film that we tested, is either comparable to or higher than the very few published zT values found in the literature for this polymer-dopant combination (see Table S8). For example, if one combines Chabinyc and colleagues' reported thermopower values [106] for vapor-doped RR-P3HT with the κ measured for vapor-doped high-M_w RR-P3HT in Ref. 21, one obtains a comparable zT value of $\approx 5 \times 10^{-3}$. Drop-cast RR-P3HT films that were blend-doped with F_4TCNQ by Zhao et al. and Kiefer et al. yielded zT values of 5×10^{-4} and 1×10^{-4}, respectively [20, 22]. Compared to our zT results for doped RR-P3HT, the fact that the zT values reported in Refs. 20 and 22 are lower by an order of magnitude is likely due to their utilization of the blend-doping method, which has been shown to yield films with poorer thermoelectric properties than those that prepared using the SqP doping method [75].

3 | Conclusions

With well-characterized film densities and specific heats and thus volumetric heat capacities, we have shown that the ambiguity in the literature regarding whether the thermal conductivity of F_4TCNQ-doped P3HT films increases or decreases upon doping relative to pristine P3HT can be understood in the context of: 1) ambiguities in the values of C_v chosen to determine κ from measured thermal diffusivity or effusivity data; 2) the extent to which the film has been doped; and, 3) the competing influences of doping-induced changes to the P3HT crystal structure and the mode localization effects of F_4TCNQ^- ion intercalation. We conclude that changes in the cross-plane κ of P3HT films as a function of doping are entirely vibrational in nature. The increase in κ at light-to-moderate doping concentrations in both RR- and RRa-P3HT is due to doping-induced crystal structural changes, specifically the doping-induced phase change of the unit cell for RR-P3HT and doping-induced crystallization in RRa-P3HT, that each enhance cross-plane heat transport. The subsequent decrease in κ at the highest doping levels result from intercalated F_4TCNQ^- ions further localizing vibrational modes within the P3HT crystallites. Finally, with accurate values for cross-plane κ, we were able to determine zT upper limits for F_4TCNQ-doped P3HT as a function of doping level. A peak zT value of 5.2×10^{-3} was determined for RR-P3HT doped with 6 mg mL^{-1} F_4TCNQ via the SqP method. Further studies are needed to map changes of C_v and κ for P3HT films doped with other molecular dopants to optimize these systems for thermoelectric applications.

4 | Experimental Section

4.1 | Poly(3-Hexylthiophene) (P3HT) Materials

We used RR-P3HT (97.6% regioregularity (RR), M_n = 28.65 kg mol^{-1}, M_w = 60.15 kg mol^{-1}, PDI = 2.1, sourced from Ossila) and RRa-P3HT (M_n = 19–34 kg mol^{-1}, M_w = 60–95 kg mol^{-1}, PDI = 2.8–3.1, sourced from Rieke Metals) to make films for TDTR, electrical conductivity, Seebeck coefficient, DSC and GIWAXS measurements. We used RR-P3HT (91%–94% regioregularity, M_n = 20–35 kg mol^{-1}, M_w = 50–70 kg mol^{-1}, PDI = 2.0–2.5, sourced from Rieke Metals) and RRa-P3HT (same as above) for bulk film density and F_4TCNQ:3HT mole ratio measurements. All of the above values for M_n, M_w, PDI and %RR were provided by the supplier and were not independently verified. The range in values of M_n and M_w were also provided by supplier Rieke Metals. Any density difference between films made from 97.6% and 91%–94% RR P3HT fall well within the density measurement error of our experiments ($\pm$ 0.04 g cm^{-3}). In addition to the measurements described in the main text, we also performed DSC measurements using the aforementioned 91%–94% RR-P3HT to test for any regioregularity dependence on C_p. We found no discernable difference in C_p between 97.6% and 91%–94% RR-P3HT in their bulk-powder morphology. However, as drop-cast films, we found that the C_p of 97.6% RR-P3HT is $\approx$10% lower than 91%–94% RR (see Table S2). See Section S1.1 for details on how we sourced all solvents, substrates and deposited metals.

4.2 | Instrumental Methods

We utilized a Perkin-Elmer DSC 8000 instrument to perform differential scanning calorimetry, a thermoanalytical technique used to measure how much energy was required to heat sample material, to determine C_p; this experiment is

described in detail in Section S1.5. We utilized an amplitude-modulated, low-pulse energy ultrafast laser system to perform time-domain thermoreflectance (TDTR), a pump-probe optical technique used to measure thermal effusivity; this experiment is described in detail in Section S1.7. We utilized a Lakeshore MeasureReady M91 FastHall system in the Van der Pauw configuration to perform four-point-probe measurements to determine electrical conductivities, and a custom-built instrument that applies thermal gradients to determine Seebeck coefficients; both of these experiments are described in detail in Section S1.8. We utilized the Synchrotron Radiation Lightsoure (SSRL) at SLAC National Accelerator Laboratory to perform grazing-incidence wide-angle x-ray scattering (GIWAXS) experiments, an x-ray diffraction technique, to characterize the nanoscale structure and morphology of polymeric thin-films; this experiment is described in detail in Section S1.9.

Acknowledgements

B.J.S. and S.H.T. gratefully acknowledge the support of the National Science Foundation under grants CHE-2305152 and DMR-2513790. R.B.W. acknowledges support from the National Science Foundation under grant CBET-1847632. Our use of the Stanford Synchrotron Radiation Lightsource, SLAC National Accelerator Laboratory, is supported by the U.S. Department of Energy, Office of Science, Office of Basic Energy Sciences under Contract No. DE-AC02-76SF00515. The authors acknowledge the staff operating beamline 11-3, especially the beamline scientists Dr. Nicholas Strange and Dr. Sarah Hesse.

Funding

NSF CHE-2305152, DMR-2513790, and CBET-1847632.

Conflicts of Interest

The authors declare no conflicts of interest.

Data Availability Statement

The data that support the findings of this study are available from the corresponding author upon reasonable request.

References

1. K. A. Peterson, E. M. Thomas, and M. L. Chabinyc, "Thermoelectric Properties of Semiconducting Polymers," *Annual Review of Materials Research* 50 (2020): 551–574.

2. G. Prunet, F. Pawula, G. Fleury, et al., "A Review on Conductive Polymers and Their Hybrids for Flexible and Wearable Thermoelectric Applications," *Materials Today Physics* 18 (2021): 100402.

3. M. V. Vedernikov and E. K. A. F. Iordanishvili, "Ioffe and Origin of Modern Semiconductor Thermoelectric Energy Conversion," in *Seventeenth International Conference on Thermoelectrics. Proceedings ICT98* (1998), 37–42.

4. H. S. Kim, W. Liu, G. Chen, C.-W. Chu, and Z. Ren, "Relationship Between Thermoelectric Figure of Merit and Energy Conversion Efficiency," *Proceedings of the National Academy of Sciences* 112 (2015): 8205–8210.

5. G. J. Snyder and A. H. Snyder, "Figure of Merit ZT of a Thermoelectric Device Defined From Materials Properties," *Energy & Environmental Science* 10 (2017): 2280–2283.

6. S. N. Patel, A. M. Glaudell, K. A. Peterson, et al., "Morphology Controls the Thermoelectric Power Factor of a Doped Semiconducting Polymer," *Science Advances* 3 (2017): 1700434.

7. J. Li, A. B. Huckleby, and M. Zhang, "Polymer-Based Thermoelectric Materials: A Review of Power Factor Improving Strategies," *Journal of Materiomics* 8 (2022): 204–220.

8. G.-H. Kim, L. Shao, K. Zhang, and K. P. Pipe, "Engineered Doping of Organic Semiconductors for Enhanced Thermoelectric Efficiency," *Nature Materials* 12 (2013): 719–723.

9. J. Liu, X. Wang, D. Li, N. E. Coates, R. A. Segalman, and D. G. Cahill, "Thermal Conductivity and Elastic Constants of PEDOT:PSS With High Electrical Conductivity," *Macromolecules* 48 (2015): 585–591.

10. A. Weathers, Z. U. Khan, R. Brooke, et al., "Significant Electronic Thermal Transport in the Conducting Poly," *Advanced Materials* 27 (2015): 2101–2106.

11. D. R. Villalva, S. Singh, L. A. Galuska, et al., "Backbone-Driven Host–Dopant Miscibility Modulates Molecular Doping in NDI Conjugated Polymers," *Materials Horizons* 9 (2022): 500–508.

12. Y. Hiroshige, M. Ookawa, and N. Toshima, "Thermoelectric Figure-of-Merit of Iodine-Doped Copolymer of Phenylenevinylene with Dialkoxyphenylenevinylene," *Synthetic Metals* 157 (2007): 467–474.

13. H. Li, M. E. DeCoster, R. M. Ireland, J. Song, P. E. Hopkins, and H. E. Katz, "Modification of the Poly(Bisdodecylquaterthiophene) Structure for High and Predominantly Nonionic Conductivity With Matched Dopants," *Journal of the American Chemical Society* 139 (2017): 11149–11157.

14. H. Li, M. E. DeCoster, C. Ming, et al., "Enhanced Molecular Doping for High Conductivity in Polymers with Volume Freed for Dopants," *Macromolecules* 52 (2019): 9804–9812.

15. J. Han, Y. Jiang, E. Tiernan, et al., "Blended Conjugated Host and Unconjugated Dopant Polymers Towards N-Type All-Polymer Conductors and High-ZT Thermoelectrics," *Angewandte Chemie International Edition* 62 (2023): 202219313.

16. O. Zapata-Arteaga, A. Perevedentsev, S. Marina, J. Martin, J. S. Reparaz, and M. Campoy-Quiles, "Reduction of the Lattice Thermal Conductivity of Polymer Semiconductors by Molecular Doping," *ACS Energy Letters* 5 (2020): 2972–2978.

17. M. He, J. Ge, Z. Lin, et al., "Thermopower Enhancement in Conducting Polymer Nanocomposites via Carrier Energy Scattering at the Organic–Inorganic Semiconductor Interface," *Energy & Environmental Science* 5 (2012): 8351–8358.

18. S. Qu, Q. Yao, L. Wang, et al., "Highly Anisotropic P3HT Films with Enhanced Thermoelectric Performance via Organic Small Molecule Epitaxy," *NPG Asia Materials* 8 (2016): 292.

19. Y. J. Jeong, J. Jung, E. H. Suh, D. Yun, J. G. Oh, and J. Jang, "Self-Healable and Stretchable Organic Thermoelectric Materials: Electrically Percolated Polymer Nanowires Embedded in Thermoplastic Elastomer Matrix," *Advanced Functional Materials* 30 (2020): 1905809.

20. H. Zhao, N. Prine, G. Ma, et al., "Out-of-Plane Transient Thermal Conductivity Measurements for Bulk Semiconducting Conjugated Polymers Using Fast Scanning Calorimetry," *Sustainable Energy & Fuels* 7 (2023): 369–380.

21. E. Plunkett, Y. Quan, B. Liao, and M. L. Chabinyc, "Blending Poly(3-Hexylthiophene) for Controlled Thermal Conductivity," *ACS Materials Letters* 6 (2024): 10–16.

22. D. Kiefer, L. Yu, E. Fransson, et al., "A Solution-Doped Polymer Semiconductor:Insulator Blend for Thermoelectrics," *Advanced Science* 4 (2017): 1600203.

23. K. Takayama, G. Ito, S. Kanazawa, R. Ikkatai, and K. Noda, "Cross-Plane Thermal Transport in Acceptor-Doped Thiophene-Based Polymer Thin Films Investigated by the 3-Omega Method," *Physica Status Solidi* 220 (2023): 2300110.

24. T. Degousée, V. Untilova, V. Vijayakumar, et al., "High Thermal Conductivity States and Enhanced Figure of Merit in Aligned Polymer Thermoelectric Materials," *Journal of Materials Chemistry A* 9 (2021): 16065–16075.

25. E. H. Suh, J. G. Oh, J. Jung, S. H. Noh, T. S. Lee, and J. Jang, "Brønsted Acid Doping of P3HT With Largely Soluble Tris(pentafluorophenyl)borane for Highly Conductive and Stable Organic Thermoelectrics Via One-Step Solution Mixing," *Advanced Energy Materials* 10 (2020): 2002521.

26. J. Sun, M.-L. Yeh, B. J. Jung, et al., "Simultaneous Increase in Seebeck Coefficient and Conductivity in a Doped Poly(alkylthiophene) Blend with Defined Density of States," *Macromolecules* 43 (2010): 2897–2903.

27. W. Zhu, X. Qiu, J. E. M. Laulainen, et al., "Enhancing the Conductivity and Thermoelectric Performance of Semicrystalline Conducting Polymers Through Controlled Tie Chain Incorporation," *Advanced Materials* 36 (2024): 2310480.

28. D. Wang, J. Ding, X. Dai, et al., "Triggering *ZT* to 0.40 by Engineering Orientation in One Polymeric Semiconductor," *Advanced Materials* 35 (2023): 2208215.

29. J. Liu, B. van der Zee, R. Alessandri, et al., "N-Type Organic Thermoelectrics: Demonstration of ZT >0.3," *Nature Communications* 11 (2020): 5694.

30. K. Kondratenko, D. Guérin, X. Wallart, S. Lenfant, and D. Vuillaume, "Thermal and Electrical Cross-Plane Conductivity at the Nanoscale in Poly(3,4-Ethylenedioxythiophene):Trifluoromethanesulfonate Thin Films," *Nanoscale* 14 (2022): 6075–6084.

31. D. Rosas Villalva, D. Derewjanko, Y. Zhang, et al., "Intermolecular-Force-Driven Anisotropy Breaks the Thermoelectric Trade-off in n-Type Conjugated Polymers," *Nature Materials* 24 (2025): 1236–1244.

32. J. Guo, K. Xu, J. Asatryan, et al., "Microstructural Evolution Dominates the Changes in the Thermal Conductivity of Conjugated Polymers Upon Doping," *Advanced Functional Materials* 36 (2025): 10822.

33. S. Ito, K. Ueji, S. Saito, et al., "Modulation of Heat Flow via Electrochemical Doping in Conducting Polymer PBTTT," *Communications Materials* 7 (2026): 145.

34. M. Chandra, Y. Zhou, C. Borges, et al., "Probing Charge-Carrier Doping Effects on Interchain Thermal Transport in Edge-on–Oriented Conjugated Polymer Thin Films," *Surfaces and Interfaces* 95 (2026): 109602.

35. P. G. Klemens and R. K. Williams, "Thermal Conductivity of Metals and Alloys," *International Metals Reviews* 31 (1986): 197–215.

36. C. Huang, X. Qian, and R. Yang, "Thermal Conductivity of Polymers and Polymer Nanocomposites," *Materials Science and Engineering: R: Reports* 132 (2018): 1–22.

37. A. Henry, "Thermal Transport in Polymers," *Annual Review of Heat Transfer* 17 (2014): 13006949.

38. S. Shen, A. Henry, J. Tong, R. Zheng, and G. Chen, "Polyethylene Nanofibres with Very High Thermal Conductivities," *Nature Nanotechnology* 5 (2010): 251–255.

39. X. Wei, Z. Wang, Z. Tian, and T. Luo, "Thermal Transport in Polymers: A Review," *Journal of Heat Transfer* 143 (2021): 072101.

40. D. Zhao, X. Qian, X. Gu, S. A. Jajja, and R. Yang, "Measurement Techniques for Thermal Conductivity and Interfacial Thermal Conductance of Bulk and Thin Film Materials," *Journal of Electronic Packaging* 138 (2016): 040802.

41. P. Jiang, X. Qian, and R. T. Yang, "Tutorial: Time-Domain Thermoreflectance (TDTR) for Thermal Property Characterization of Bulk and Thin Film Materials," *Journal of Applied Physics* 124 (2018): 161103.

42. Y. S. Ju, K. Kurabayashi, and K. E. Goodson, "Thermal Characterization of Anisotropic Thin Dielectric Films Using Harmonic Joule Heating," *Thin Solid Films* 339 (1999): 160–164.

43. J. P. Feser and D. G. Cahill, "Probing Anisotropic Heat Transport Using Time-Domain Thermoreflectance with Offset Laser Spots," *Review of Scientific Instruments* 83 (2012): 104901.

44. P. Jiang, X. Qian, and R. Yang, "Time-Domain Thermoreflectance (TDTR) Measurements of Anisotropic Thermal Conductivity Using a Variable Spot Size Approach," *Review of Scientific Instruments* 88 (2017): 074901.

45. P. Jiang, X. Qian, and R. Yang, "A New Elliptical-Beam Method Based on Time-Domain Thermoreflectance (TDTR) to Measure the in-Plane Anisotropic Thermal Conductivity and Its Comparison with the Beam-Offset Method," *Review of Scientific Instruments* 89 (2018): 094902.

46. D. M. DeLongchamp, B. M. Vogel, Y. Jung, et al., "Variations in Semiconducting Polymer Microstructure and Hole Mobility With Spin-Coating Speed," *Chemistry of Materials* 17 (2005): 5610–5612.

47. H. Yang, S. W. LeFevre, C. Y. Ryu, and Z. Bao, "Solubility-Driven Thin Film Structures of Regioregular Poly(3-Hexyl Thiophene) Using Volatile Solvents," *Applied Physics Letters* 90 (2007): 172116.

48. X. Feng, G. Liu, S. Xu, H. Lin, and X. Wang, "3-Dimensional Anisotropic Thermal Transport in Microscale Poly(3-Hexylthiophene) Thin Films," *Polymer* 54 (2013): 1887–1895.

49. Q. Wei, C. Uehara, M. Mukaida, K. Kirihara, and T. Ishida, "Measurement of in-Plane Thermal Conductivity in Polymer Films," *AIP Advances* 6 (2016): 045315.

50. H. Ushirokita and H. Tada, "In-Plane Thermal Conductivity Measurement of Conjugated Polymer Films by Membrane-Based AC Calorimetry," *Chemistry Letters* 45 (2016): 735–737.

51. S. Kommandur and S. Yee, "A Suspended 3-Omega Technique to Measure the Anisotropic Thermal Conductivity of Semiconducting Polymers," *Review of Scientific Instruments* 89 (2018): 114905.

52. C. O. Diarra, C. Massobrio, and E. Martin, "Heat Transfer Through Covalent versus Non-Covalent Bonding: A Case Study on Crystalline π-Conjugated P3HT Polymer using Approach-to-Equilibrium Molecular Dynamics," *Physical Chemistry Chemical Physics* 27 (2025): 18487–18495.

53. A. J. Heeger, "Semiconducting Polymers: The Third Generation," *Chemical Society Reviews* 39 (2010): 2354–2371.

54. M. P. Bhatt, H. D. Magurudeniya, E. A. Rainbolt, et al., "Poly(3-Hexylthiophene) Nanostructured Materials for Organic Electronics Applications," *Journal of Nanoscience and Nanotechnology* 14 (2014): 1033–1050.

55. A. T. Kleinschmidt, S. E. Root, and D. J. Lipomi, "Poly(3-Hexylthiophene) (P3HT): Fruit Fly or Outlier in Organic Solar Cell Research?," *Journal of Materials Chemistry A* 5 (2017): 11396–11400.

56. C. S. Lee and M. D. Dadmun, "Important Thermodynamic Characteristics of Poly(3-Hexyl Thiophene)," *Polymer* 55 (2014): 4–7.

57. X. Shen, W. Hu, and T. P. Russell, "Measuring the Degree of Crystallinity in Semicrystalline Regioregular Poly(3-Hexylthiophene)," *Macromolecules* 49 (2016): 4501–4509.

58. R. Xie, A. R. Weisen, Y. Lee, et al., "Glass Transition Temperature From the Chemical Structure of Conjugated Polymers," *Nature Communications* 11 (2020): 893.

59. R. Remy, S. Wei, L. M. Campos, and M. E. Mackay, "Three-Phase Morphology of Semicrystalline Polymer Semiconductors: A Quantitative Analysis," *ACS Macro Letters* 4 (2015): 1051–1055.

60. J. Balko, R. H. Lohwasser, M. Sommer, M. Thelakkat, and T. Thurn-Albrecht, "Determination of the Crystallinity of Semicrystalline Poly(3-Hexylthiophene) by Means of Wide-Angle X-Ray Scattering," *Macromolecules* 46 (2013): 9642–9651.

61. S. Hugger, R. Thomann, T. Heinzel, and T. Thurn-Albrecht, "Semicrystalline Morphology in Thin Films of Poly(3-Hexylthiophene)," *Colloid and Polymer Science* 282 (2004): 932–938.

62. P. S. O. Patrício, H. D. R. Calado, F. A. C. D. Oliveira, et al., "Correlation Between Thermal, Optical and Morphological Properties

of Heterogeneous Blends of Poly(3-Hexylthiophene) and Thermoplastic Polyurethane," *Journal of Physics-Condensed Matter* 18 (2006): 7529–7542.

63. S. Hiura, N. Okada, J. Wakui, H. Narita, S. Kanehashi, and T. Shimomura, "Thermoelectric Properties of Poly(3-Hexylthiophene) Nanofiber Mat With a Large Void Fraction," *Materials* 10 (2017): 468.

64. Z. Wu, A. Petzold, T. Henze, et al., "Temperature and Molecular Weight Dependent Hierarchical Equilibrium Structures in Semiconducting Poly(3-Hexylthiophene)," *Macromolecules* 43 (2010): 4646–4653.

65. P. Zhan, W. Zhang, I. E. Jacobs, et al., "Side Chain Length Affects Backbone Dynamics in Poly(3-Alkylthiophene)s," *Journal of Polymer Science Part B: Polymer Physics* 56 (2018): 1193–1202.

66. D. G. Cahill, "Analysis of Heat Flow in Layered Structures for Time-Domain Thermoreflectance," *Review of Scientific Instruments* 75 (2004): 5119–5122.

67. M. J. Gomez, K. Liu, J. G. Lee, and R. B. Wilson, "High Sensitivity Pump–Probe Measurements of Magnetic, Thermal, and Acoustic Phenomena with a Spectrally Tunable Oscillator," *Review of Scientific Instruments* 91 (2020): 023905.

68. M. S. B. Hoque, Y. R. Koh, K. Aryana, et al., "Thermal Conductivity Measurements of Sub-Surface Buried Substrates by Steady–State Thermoreflectance," *Review of Scientific Instruments* 92 (2021): 064906.

69. R. Mohan, S. Khan, R. B. Wilson, and P. E. Hopkins, "Time-Domain Thermoreflectance," *Nature Reviews Methods Primers* 5 (2025): 55.

70. N. Yaghoobi Nia, M. Bonomo, M. Zendehdel, et al., "Impact of P3HT Regioregularity and Molecular Weight on the Efficiency and Stability of Perovskite Solar Cells," *ACS Sustainable Chemistry & Engineering* 9 (2021): 5061–5073.

71. M. Azhar Ansari, S. Mohiuddin, and F. Kandemirli, "Imran Malik, M. Synthesis and Characterization of Poly(3-Hexylthiophene): Improvement of Regioregularity and Energy Band Gap," *RSC Advances* 8 (2018): 8319–8328.

72. Y. Lee, A. Mongare, A. Plant, and D. Ryu, "Strain–Microstructure–Optoelectronic Inter-Relationship Toward Engineering Mechano-Optoelectronic Conjugated Polymer Thin Films," *Polymers* 13 (2021): 935.

73. C. R. Snyder, J. S. Henry, and D. M. DeLongchamp, "Effect of Regioregularity on the Semicrystalline Structure of Poly(3-Hexylthiophene)," *Macromolecules* 44 (2011): 7088–7091.

74. J.-S. Kim, J.-H. Kim, W. Lee, et al., "Tuning Mechanical and Optoelectrical Properties of Poly(3-Hexylthiophene) Through Systematic Regioregularity Control," *Macromolecules* 48 (2015): 4339–4346.

75. D. T. Scholes, S. A. Hawks, P. Y. Yee, et al., "Overcoming Film Quality Issues for Conjugated Polymers Doped with F_4 TCNQ by Solution Sequential Processing: Hall Effect, Structural, and Optical Measurements," *The Journal of Physical Chemistry Letters* 6 (2015): 4786–4793.

76. D. T. Scholes, P. Y. Yee, J. R. Lindemuth, et al., "The Effects of Crystallinity on Charge Transport and the Structure of Sequentially Processed F_4 TCNQ-Doped Conjugated Polymer Films," *Advanced Functional Materials* 27 (2017): 1702654.

77. A. Hamidi-Sakr, L. Biniek, J. Bantignies, et al., "A Versatile Method to Fabricate Highly In-Plane Aligned Conducting Polymer Films With Anisotropic Charge Transport and Thermoelectric Properties: The Key Role of Alkyl Side Chain Layers on the Doping Mechanism," *Advanced Functional Materials* 27 (2017): 1700173.

78. J. Hynynen, D. Kiefer, L. Yu, et al., "Enhanced Electrical Conductivity of Molecularly P-Doped Poly(3-Hexylthiophene) Through Understanding the Correlation With Solid-State Order," *Macromolecules* 50 (2017): 8140–8148.

79. V. Untilova, T. Biskup, L. Biniek, V. Vijayakumar, and M. Brinkmann, "Control of Chain Alignment and Crystallization Helps Enhance Charge Conductivities and Thermoelectric Power Factors in Sequentially Doped P3HT:F_4 TCNQ Films," *Macromolecules* 53 (2020): 2441–2453.

80. V. Untilova, H. Zeng, P. Durand, L. Herrmann, N. Leclerc, and M. Brinkmann, "Intercalation and Ordering of F_6 TCNNQ and F_4 TCNQ Dopants in Regioregular Poly(3-Hexylthiophene) Crystals: Impact on Anisotropic Thermoelectric Properties of Oriented Thin Films," *Macromolecules* 54 (2021): 6073–6084.

81. Y. Wu, Q. M. Duong, A. F. Simafranca, C. Z. Salamat, B. J. Schwartz, and S. H. Tolbert, "Crystal Structure Control of the Energetics of Chemical Doping in Rub-Aligned P3HT Films," *ACS Materials Letters* 6 (2024): 489–497.

82. P. Y. Yee, D. T. Scholes, B. J. Schwartz, and S. H. Tolbert, "Dopant-Induced Ordering of Amorphous Regions in Regiorandom P_3HT," *The Journal of Physical Chemistry Letters* 10 (2019): 4929–4934.

83. Y. Wu, C. Z. Salamat, A. León Ruiz, et al., "Using Bulky Dodecaborane-Based Dopants to Produce Mobile Charge Carriers in Amorphous Semiconducting Polymers," *Chemistry of Materials* 36 (2024): 5552–5562.

84. P. Pingel and D. Neher, "Comprehensive Picture of *p*-Type Doping of P3HT with the Molecular Acceptor F_4TCNQ," *Physical Review B* 87 (2013): 115209.

85. P. Pingel, M. Arvind, L. Kölln, et al., "*p*-Type Doping of Poly(3-Hexylthiophene) with the Strong Lewis Acid Tris(Pentafluorophenyl)Borane," *Advanced Electronic Materials* 2 (2016): 1600204.

86. T. J. Aubry, J. C. Axtell, V. M. Basile, et al., "Dodecaborane-Based Dopants Designed to Shield Anion Electrostatics Lead to Increased Carrier Mobility in a Doped Conjugated Polymer," *Advanced Materials* 31 (2019): 1805647.

87. J. A. Malen, K. Baheti, T. Tong, Y. Zhao, J. A. Hudgings, and A. Majumdar, "Optical Measurement of Thermal Conductivity Using Fiber Aligned Frequency Domain Thermoreflectance," *Journal of Heat Transfer* 133 (2011): 081601.

88. J. C. Duda, P. E. Hopkins, Y. Shen, and M. C. Gupta, "Thermal Transport in Organic Semiconducting Polymers," *Applied Physics Letters* 102 (2013): 251912.

89. 2,3,5,6-Tetrafluoro-7,7',8,8'-tetracyanoquinodimethane; MSDS UPF01017 [Online]; Shanghai Up- Fluorochem Co., Ltd.: August 11, 2017.

90. A. Roy, T. L. Bougher, R. Geng, Y. Ke, J. Locklin, and B. A. Cola, "Thermal Conductance of Poly(3-Methylthiophene) Brushes," *ACS Applied Materials & Interfaces* 8 (2016): 25578–25585.

91. K. Herrmann, S. Freund, F. Eller, et al., "Microstructural and Thermal Transport Properties of Regioregular Poly(3-Hexylthiophene-2,5-Diyl) Thin Films," *Materials* 15 (2022): 7700.

92. X. Rodríguez-Martínez, F. Saiz, B. Dörling, et al., "On the Thermal Conductivity of Conjugated Polymers for Thermoelectrics," *Advanced Energy Materials* 14 (2024): 2401705.

93. S. Rausch, D. Rauh, C. Deibel, S. Vidi, and H. P. Ebert, "Thin-Film Thermal-Conductivity Measurement on Semi-Conducting Polymer Material Using the 3ω Technique," *International Journal of Thermophysics* 34 (2013): 820–830.

94. D. G. Cahill, M. Katiyar, and J. R. Abelson, "Thermal Conductivity of A-Si:H Thin Films," *Physical Review B* 50 (1994): 6077–6081.

95. J. H. Kim, A. Feldman, and D. Novotny, "Application of the Three Omega Thermal Conductivity Measurement Method to a Film on a Substrate of Finite Thickness," *Journal of Applied Physics* 86 (1999): 3959–3963.

96. R. Franz and G. Wiedemann, "Ueber die Wärme-Leitungsfähigkeit der Metalle," *Annalen der Physik* 165 (1853): 497–531.

97. A. Yadav, P. C. Deshmukh, K. Roberts, N. M. Jisrawi, and S. R. Valluri, "An Analytic Study of the Wiedemann–Franz Law and the Thermoelectric Figure of Merit," *Journal of Physics Communications* 3 (2019): 105001.

98. C. Nath, A. Kumar, K.-Z. Syu, and Y.-K. Kuo, "Heat Conduction in Conducting Polyaniline Nanofibers," *Applied Physics Letters* 103 (2013): 121905.

99. X. Xu, J. Zhou, and J. Chen, "Thermal Transport in Conductive Polymer–Based Materials," *Advanced Functional Materials* 30 (2020): 1904704.

100. D. G. Cahill and R. O. Pohl, "Heat Flow and Lattice Vibrations in Glasses," *Solid State Communications* 70 (1989): 927–930.

101. D. G. Cahill, S. K. Watson, and R. O. Pohl, "Lower Limit to the Thermal Conductivity of Disordered Crystals," *Physical Review B* 46 (1992): 6131–6140.

102. W.-P. Hsieh, M. D. Losego, P. V. Braun, S. Shenogin, P. Keblinski, and D. G. Cahill, "Testing the Minimum Thermal Conductivity Model for Amorphous Polymers Using High Pressure," *Physical Review B* 83 (2011): 174205.

103. X. Xie, K. Yang, D. Li, et al., "High and Low Thermal Conductivity of Amorphous Macromolecules," *Physical Review B* 95 (2017): 035406.

104. P. B. Allen and J. L. Feldman, "Thermal Conductivity of Disordered Harmonic Solids," *Physical Review B* 48 (1993): 12581–12588.

105. P. B. Allen, J. L. Feldman, J. Fabian, and F. D. Wooten, "Diffusons, Locons and Propagons: Character of Atomic Vibrations in Amorphous Si," *Philosophical Magazine B* 79 (1999): 1715–1731.

106. E. Lim, K. A. Peterson, G. M. Su, and M. L. Chabinyc, "Thermoelectric Properties of Poly(3-hexylthiophene) (P3HT) Doped with 2,3,5,6-Tetrafluoro-7,7,8,8-tetracyanoquinodimethane (F_4TCNQ) by Vapor-Phase Infiltration," *Chemistry of Materials* 30 (2018): 998–1010.

Supporting Information

Additional supporting information can be found online in the Supporting Information section.

Supporting File: adfm76788-sup-0001-SuppMat.docx.